

Positive linear magnetoresistance effect in disordered $L2_1B$ -type Mn_2CoAl epitaxial filmsK. Kudo,¹ A. Masago,² S. Yamada,^{2,1} L. S. R. Kumara,³ H. Tajiri,³ Y. Sakuraba,⁴ K. Hono,⁴ and K. Hamaya^{2,1,*}¹*Department of Systems Innovation, Graduate School of Engineering Science, Osaka University, Toyonaka, Osaka 560-8531, Japan*²*Center for Spintronics Research Network, Graduate School of Engineering Science, Osaka University, Toyonaka, Osaka 560-8531, Japan*³*Center for Synchrotron Radiation Research, Japan Synchrotron Radiation Research Institute, 1-1-1 Kouto, Sayo, Hyogo 679-5198, Japan*⁴*Research Center for Magnetic and Spintronics Materials, National Institute for Materials Science, 1-2-1 Sengen, Tsukuba 305-0047, Japan*

(Received 15 October 2020; accepted 23 February 2021; published 17 March 2021)

The inverse Heusler alloy Mn_2CoAl is known as a spin gapless semiconductor (SGS). It is believed that the positive linear magnetoresistance (PLMR) effect observed at low temperatures indicates the quantum linear MR effect in the gapless electronic band structures near the Fermi level, i.e., evidence of the realization of a SGS [Ouardi *et al.*, *Phys. Rev. Lett.* **110**, 100401 (2013)]. For this reason, one presumes that the observation of the PLMR effect is indirect proof of the demonstration of XA -type Mn_2CoAl consisting of the inverse Heusler structure. In this paper, we observe the PLMR effect at 10 K in homogeneous and single-phase Mn_2CoAl epitaxial films grown by low-temperature molecular beam epitaxy at 100 °C. From anomalous x-ray diffraction measurements and analyses, we clarify that the 100 °C-grown Mn_2CoAl epitaxial film is not composed of the XA -type structure but a disordered $L2_1B$ -type structure including some amount of Mn(A site) \leftrightarrow Co(C site) swapping and Mn(B site) \leftrightarrow Al(D site) swapping. On the basis of first-principles density-functional theory calculations, we discuss the correlation between the PLMR effect observed at 10 K and the possible electronic band structure in the disordered $L2_1B$ -type Mn_2CoAl .

DOI: [10.1103/PhysRevB.103.104427](https://doi.org/10.1103/PhysRevB.103.104427)**I. INTRODUCTION**

The spin gapless semiconductor (SGS) is a new class of semiconductors with the zero-gap electronic band structure near the Fermi level in one spin channel and the usual finite band gap structure in another spin channel [1,2]. In the research field of spintronics [3], the special electronic band structure is expected to offer unique properties of both high-mobility zero-gap semiconductors and half-metallic materials. If SGSs are realized, one can utilize these as highly efficient spin injectors and highly spin-polarized channels with tunable magnetic properties by applying an electric field [1,2]. Very recently, some novel applications such as a reconfigurable magnetic tunnel diode and transistor structures were also proposed [4,5].

To date, candidate materials such as Co- or Mn-doped $PdPbO_2$ [1,6], graphene nanoribbons [2,7], silicene nanoribbons [8], $MoSn$ [9], and some Heusler alloys [10–17] have been predicted as SGSs. As unique physical properties in SGSs, (i) weak temperature-dependent conductivity (resistivity), (ii) high spin polarization, (iii) a vanishing Seebeck coefficient, and (iv) the positive linear magnetoresistance (PLMR) effect derived from the quantum linear MR effect [18] have been reported for Co-doped $PdPbO_2$ [19] and several Heusler alloys [10,20–26].

As a spintronic material, one of the ternary Heusler alloys, Mn_2CoAl , is a popular SGS because the above SGS-like physical properties were first reported in a bulk sample in 2013 [10]. Notably, it is believed that the Hg_2TiCu -type inverse

Heusler (XA -type) structure is essential to realize the electronic band structure showing SGS-like physical properties [27]. In the first report of the bulk Mn_2CoAl [10], a magnetic moment of $\sim 2.0 \mu_B/f.u.$, consistent with the theoretical prediction, was demonstrated. In addition, the weak negative (positive) temperature dependence of electrical resistivity ρ (conductivity), a very small anomalous Hall conductivity σ_{AHC} of 21.8 S/cm, and the PLMR effect arising from the quantum linear MR effect at low temperatures were observed. Up to now, many groups have tried to achieve Mn_2CoAl films for spintronic devices, and weak negative temperature-dependent ρ and small σ_{AHC} values have also been observed [28–34]. However, the PLMR effect at low temperatures for Mn_2CoAl films has never been observed.

Very recently, Xu *et al.* investigated the atomic-level ordered structure, electrical, and magnetic properties for bulk Mn_2CoAl samples in detail [35], where high-angle annular dark-field scanning transmission electron microscopy (HAADF-STEM) and anomalous x-ray diffraction (AXRD) measurements were used to distinguish the structural difference between the XA -type structure and conventional $L2_1$ -type structure. Even for the bulk Mn_2CoAl samples including inhomogeneous and disordered structures, they observed the weak negative temperature-dependent ρ and small σ_{AHC} values. From the detailed comparisons, one can see that there is no correlation among the weak negative temperature-dependent ρ , small σ_{AHC} values, and the formation of the XA -type structure that is essential to the SGS electronic band structure [27].

In this paper, we experimentally observe the PLMR effect at 10 K in homogeneous and single-phase Mn_2CoAl epitaxial films grown by low-temperature molecular beam

*hamaya@ee.es.osaka-u.ac.jp

epitaxy (MBE) at 100 °C. In addition to the simple structural, electrical, and magnetotransport characterizations, we perform AXRD measurements and analyses for the 100 °C-grown Mn₂CoAl epitaxial film. As a result, we find that the 100 °C-grown Mn₂CoAl epitaxial film is not composed of an *XA*-type structure but a disordered *L2₁B*-type structure having some amount of Mn(A site) \leftrightarrow Co(C site) swapping and Mn(B site) \leftrightarrow Al(D site) swapping. On the basis of the structure determined here, we discuss the correlation between the PLMR effect and a possible electronic band structure calculated by the first-principles density-functional theory. We suggest that there is no correlation between the presence of the PLMR effect at low temperatures and the realization of the *XA*-type structure in Mn₂CoAl.

II. FILM GROWTH AND MEASUREMENTS

Schematics of the crystal structures considered for Mn₂CoAl are shown in Fig. 1(a) [10,27,35–37]. As shown in the left panel, when Mn atoms occupy A(0, 0, 0) and B($\frac{1}{4}$, $\frac{1}{4}$, $\frac{1}{4}$) sites and Co atoms and Al atoms occupy C($\frac{1}{2}$, $\frac{1}{2}$, $\frac{1}{2}$) and D($\frac{3}{4}$, $\frac{3}{4}$, $\frac{3}{4}$) sites, respectively, the crystal structure is the so-called *XA*-type structure, leading to SGS-like electronic band structures [10,27]. The A, B, C, and D sites correspond to the following Wyckoff positions: *4a*, *4c*, *4b*, and *4d*, respectively. When Mn and Co atoms randomly occupy the A and C sites and Mn atoms occupy the B site, as shown in the right panel, it becomes an *L2₁B*-type structure, which is not a SGS [27,36]. Notably, there is no report on direct evidence of the formation of the *XA*-type structure for Mn₂CoAl up to now.

In this study, Mn₂CoAl films were grown on MgAl₂O₄(001) substrates (sample size: 1 × 1 cm²) by nonstoichiometric MBE techniques [32,38–42], where the film thickness was tuned to be 3.5, 15, and 50 nm according to each measurement. Since the mismatch between the lattice constant of Mn₂CoAl and the half diagonal length of the lattice constant of MgAl₂O₄ ($0.808 \text{ nm} \times 1/\sqrt{2} = 0.571 \text{ nm}$) is $\sim 1.5\%$ [32], we can expect an epitaxial relationship of Mn₂CoAl[100](001)//MgAl₂O₄[110](001). For the film growth, the MgAl₂O₄(001) substrates used here were chemically cleaned by Semico Clean 56 (Furuuchi Chemical) and then were loaded into an MBE chamber, followed by the heat treatment at 600 °C for 1 h under a base pressure of $\sim 10^{-7}$ Pa. From *in situ* reflection high-energy electron diffraction (RHEED) observations, good surface flatness on the used MgAl₂O₄(001) substrate was confirmed (not shown here). After that, we set a growth temperature of 100 °C and grew Mn₂CoAl films by coevaporating Mn, Co, and Al using Knudsen cells, where the supplied atomic composition ratio of Mn:Co:Al was 2.0:1.1:2.0 during the growth [32]. Structural characterizations were carried out by *in situ* RHEED, XRD, AXRD, HAADF-STEM, and energy-dispersive x-ray spectroscopy (EDX).

To measure electrical and magnetotransport properties, the grown Mn₂CoAl films were patterned into Hall-bar devices with 80- μm width and 400- μm length (as shown in the inset of Fig. 3 below) by conventional photolithography and Ar ion-milling techniques. Electrical and magnetotransport properties were measured using a four-terminal dc method in a

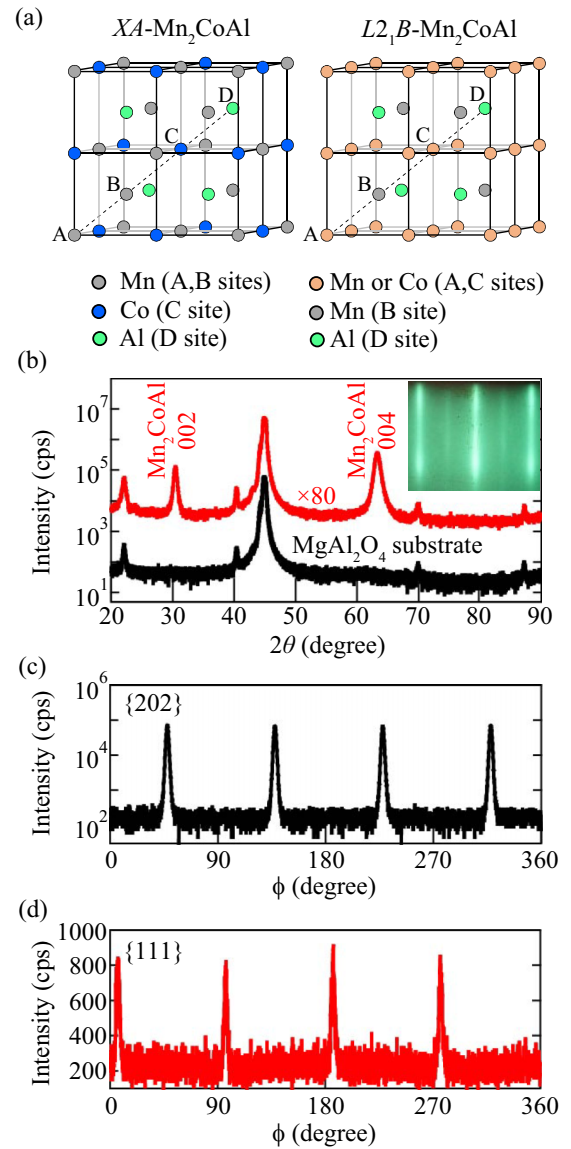


FIG. 1. (a) Crystal structures of inverse Heusler *XA*-type (left) and *L2₁B*-type (right) Mn₂CoAl. The A, B, C, and D sites correspond to *4a*, *4c*, *4b*, and *4d* Wyckoff positions, respectively. (b) θ - 2θ XRD pattern of the 100 °C-grown Mn₂CoAl film grown on MgAl₂O₄(001) (red), together with that for a MgAl₂O₄(001) substrate (black). The inset shows a RHEED image of the Mn₂CoAl surface after the growth. (c) and (d) XRD ϕ -scan profiles in {202} and {111}, respectively, for the 100 °C-grown Mn₂CoAl film.

physical property measurement system (Quantum Design) at various temperatures. External magnetic fields were perpendicular (B_z) and parallel (B_y) to the film plane for Hall-effect and MR measurements, respectively.

III. RESULTS

A. Conventional structural characterizations

During the growth of 100 °C-grown Mn₂CoAl films, we observe the *in situ* RHEED image of the symmetrical streaks [inset of Fig. 1(b)], indicating good two-dimensional epitaxial growth of the Mn₂CoAl films. Figure 1(b) shows a conventional θ - 2θ XRD pattern for the 100 °C-grown Mn₂CoAl film

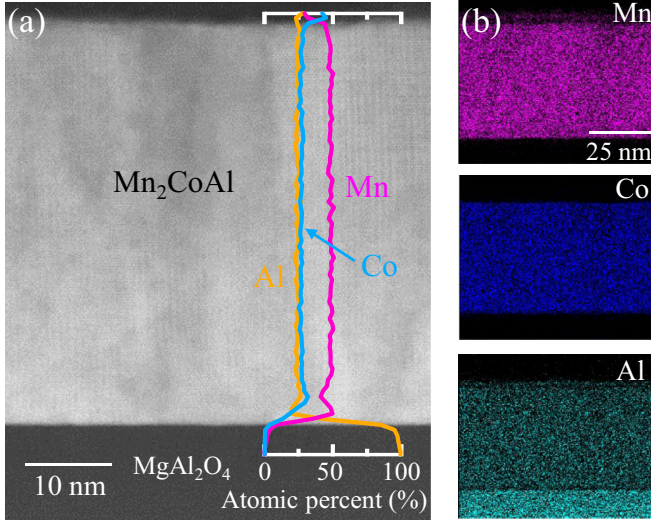


FIG. 2. (a) HAADF-STEM image of the 100 °C-grown Mn_2CoAl film on $\text{MgAl}_2\text{O}_4(001)$, together with EDX line profiles of Mn, Co, Al. (b) EDX elemental maps of Mn, Co, and Al for the same $\text{Mn}_2\text{CoAl}/\text{MgAl}_2\text{O}_4(001)$ heterostructure.

(red), together with that for a $\text{MgAl}_2\text{O}_4(001)$ substrate (black) using $\text{Cu } K\alpha$ radiation at 0.15418 nm. In addition to the diffraction peaks originating from MgAl_2O_4 substrates, the 002 and 004 diffraction peaks from Mn_2CoAl are clearly observed at 2θ values of $\sim 30^\circ$ and $\sim 63^\circ$, respectively, indicating the formation of [001]-oriented epitaxial Mn_2CoAl films. The lattice constant is estimated to be ~ 0.588 nm, comparable to a reported bulk sample (~ 0.584 nm) [35] and low-temperature ($\leq 300^\circ\text{C}$) grown films (0.586–0.587 nm) [32,33], while these values are slightly larger than the theoretical value of 0.576–0.577 nm [32,36]. From the XRD ϕ -scan profile in {202} for the Mn_2CoAl film in Fig. 1(c), the in-plane crystal orientation of $\text{Mn}_2\text{CoAl}[100](001)/\text{MgAl}_2\text{O}_4[110](001)$ is confirmed. Figure 1(d) shows an XRD ϕ -scan profile in {111} for the 100 °C-grown Mn_2CoAl film. Sharp diffraction peaks with fourfold symmetry are clearly seen, indicating the formation of an XA - or $L2_1B$ -type structure in the 100 °C-grown Mn_2CoAl films. From the comparisons of these intensities, we roughly estimate the degree of $B2$ and $L2_1$ ordering, S_{B2} and S_{L2_1} , for the Mn_2CoAl films from the following equations [43,44]:

$$S_{B2} = \sqrt{\frac{I_{002}/I_{004}}{I_{002}^R/I_{004}^R}}, \quad S_{L2_1} = \frac{2}{3 - S_{B2}} \sqrt{\frac{I_{111}/I_{202}}{I_{111}^R/I_{202}^R}}, \quad (1)$$

where I_{hkl} and I_{hkl}^R are the experimental and theoretical peak intensities for the hkl plane. As a result, the values of S_{B2} and S_{L2_1} are ~ 1 and ~ 0.4 , respectively. These results indicate that the 100 °C-grown Mn_2CoAl films include some amount of Mn(B site) and Al(D site) disorder.

Figure 2 shows a typical HAADF-STEM image of the 100 °C-grown Mn_2CoAl film, together with the results of the EDX line scan and elemental maps. In the HAADF-STEM image, the contrast within the Mn_2CoAl layer is uniform, indicating a compositionally homogeneous and single-phase film over the measured area. According to the EDX line profiles

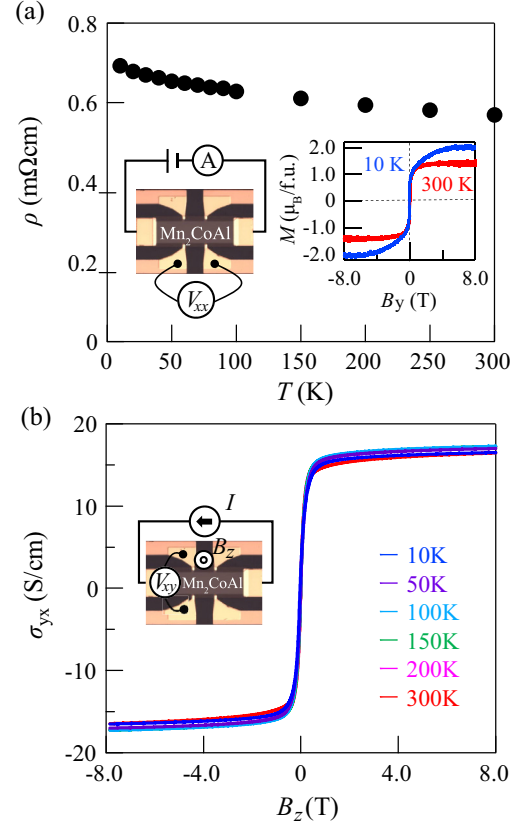


FIG. 3. (a) Temperature dependence of the electrical resistivity ρ and (b) Hall conductivity σ_{yx} as a function of out-of-plane external magnetic fields at various temperatures for the 100 °C-grown Mn_2CoAl film. The inset pictures show micrographs of the fabricated Hall-bar devices including the measurement scheme and M - B_y curve at 10 and 300 K for the 100 °C-grown Mn_2CoAl film.

from the $\text{Mn}_2\text{CoAl}/\text{MgAl}_2\text{O}_4(001)$ interface, the chemical composition in the Mn_2CoAl layer along the vertical direction is almost stoichiometric (Mn:Co:Al = 2:1:1) [Fig. 2(a)]. The EDX elemental maps in Fig. 2(b) indicate the absence of the phase separation in the 100 °C-grown Mn_2CoAl films. From these structural characterizations, homogeneous and single-phase Mn_2CoAl epitaxial films are demonstrated even at an extremely low growth temperature of 100 °C.

B. Electrical resistivity and anomalous Hall conductivity

Figure 3(a) shows the temperature dependence of ρ for 3.5-nm-thick Mn_2CoAl films, together with magnetization curves measured at 10 and 300 K in the inset. Weak negative temperature-dependent ρ , similar to those observed for the bulk [10,35] and thin-film samples [29–34], is observed. In addition, magnetic moments at 10 K and at 300 K are almost the same as those for the bulk in Ref. [10] and for epitaxial films in Ref. [32].

The magnetic-field (B_z) dependence of the Hall conductivity σ_{yx} at various temperatures is displayed in Fig. 3(b). A small temperature dependence of σ_{yx} , similar to the temperature dependence of ρ in Fig. 3(a), is also observed. The value of σ_{AHC} can be estimated to be ~ 16 S/cm, comparable to that

for thin-film samples [28,32], from the extrapolation of the σ_{yx} - B_z curve above 7.0 T towards zero field. Such small values of σ_{AHC} were theoretically explained by the electronic band structure of Mn_2CoAl [10,32]. Although the homogeneous and single-phase Mn_2CoAl epitaxial films with an XA - or $L2_1B$ -type structure were confirmed in Sec. III A, the above features in Fig. 3 are not evidence of the formation of XA -type Mn_2CoAl [32,35].

We also estimate the value of carrier concentration p by using the single-band model, $p = 1/qR_H$, where q is the elemental charge and R_H is the Hall coefficient estimated from the slope of Hall voltages at high magnetic fields (≥ 7.0 T) after subtracting the anomalous Hall component. For the 100 °C-grown homogeneous and single-phase Mn_2CoAl epitaxial films, the normal Hall voltage is positive, indicating the charge carriers are holes. Also, the values of p are estimated to be $\sim 1.9 \times 10^{22} \text{ cm}^{-3}$ at 300 K and $\sim 2.0 \times 10^{22} \text{ cm}^{-3}$ at 10 K, two orders of magnitude higher than those of the polycrystalline bulk Mn_2CoAl [10]. We speculate that there are some disordered structures, resulting in the high carrier concentration, in the 100 °C-grown Mn_2CoAl films [27,32]. These results were reproducibly observed for 15- and 50-nm-thick Mn_2CoAl epitaxial films.

C. Magnetoresistance

We focus on the magnetoresistance (MR) effect of the 100 °C-grown Mn_2CoAl epitaxial films. In general, MR in ferromagnetic materials exhibits negative changes due to the suppression of the spin-dependent carrier scattering with increasing H [45,46]. Above T_C , the positive changes in the MR, attributed to the carrier scattering derived from Lorentz force with increasing H , can be observed, where the Lorentz force is proportional to the square of H [47]. However, for bulk Mn_2CoAl [10], it was reported that the PLMR effect arising from the quantum linear MR effect described elsewhere [18,48] was observed. In fact, the quantum linear MR effect was observed for various zero-gap materials [49–52].

Figure 4 shows the field-dependent MR ratio for a 3.5-nm-thick Mn_2CoAl epitaxial film at various temperatures, where the MR ratio is defined as $\{[R_{xx}(B_y) - R_{xx}(0)]/R_{xx}(0)\} \times 100\%$, with $R_{xx}(B_y)$ and $R_{xx}(0)$ being the electrical resistance with and without applying in-plane external magnetic fields B_y , respectively. With varying the measurement temperature from 50 to 10 K, the MR features markedly change from negative to positive, and the PLMR effect is clearly observed at 10 K, which is reproduced for another 100 °C-grown Mn_2CoAl film, as shown in the inset. Because the 100 °C-grown Mn_2CoAl epitaxial film shows a ferromagnetic nature at 10 K, as shown in the inset of Fig. 3(a), we speculate that the observed PLMR effect arises from the quantum linear MR effect due to the special electronic structure near the Fermi level at this stage [18,48].

However, the size of the MR ratio observed in Fig. 4 was much smaller than those observed in previous work on the bulk Mn_2CoAl [10]. It has been discussed that the size of the MR ratio depends on the carrier mobility [51]. A similar feature has already been observed for low-temperature-grown $CoFeVSi$ epitaxial films [23]. From these results, although we can conclude that homogeneous and single-phase Mn_2CoAl

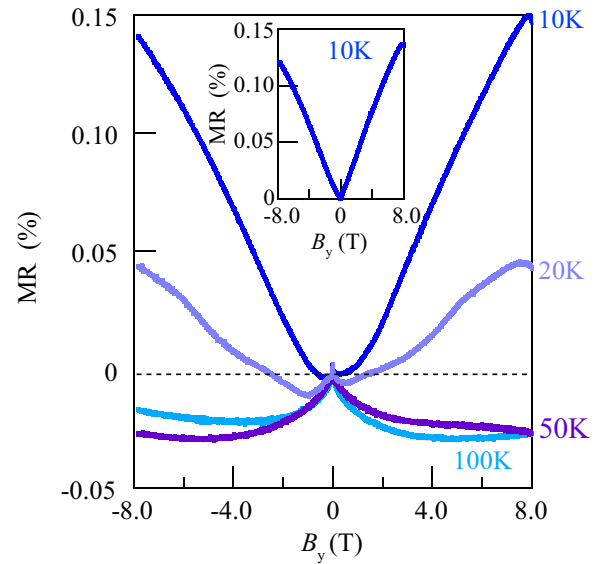


FIG. 4. Magnetoresistance (MR) ratio as a function of in-plane external magnetic fields at various temperatures. The inset shows an MR curve for another device at 10 K.

epitaxial films evidently show the PLMR effect at 10 K, there is still no evidence of the formation of the XA -type structure.

D. Atomic-level ordered structure

By using AXRD measurements and analyses [35,53–55], we first focus on the microscopic structure of the 100 °C-grown Mn_2CoAl films, where the AXRD measurement was performed at the standard undulator beamline BL13XU in SPring-8 using a six-circle diffractometer [56,57]. To evaluate the atomic structures of the Mn_2CoAl film without ambiguity, we need at least two intensity sets, i.e., I_{002}/I_{004} and I_{111}/I_{004} [58]. Prior to the detailed measurements, we calculate the x-ray energy dependence of integrated intensities of 004(I_{004}), 002(I_{002}), and 111(I_{111}) reflections from 6.3 to 6.7 keV around the Mn K absorption edge (~ 6.54 keV) of XA -type Mn_2CoAl . The solid curves in Figs. 5(a) and 5(b) show the x-ray energy dependence of the calculated intensities of I_{002}/I_{004} with Mn(B site) \leftrightarrow Co(C site) disorder and I_{111}/I_{004} with Mn(A site) \leftrightarrow Co(C site) disorder near the Mn K absorption edge of XA -type Mn_2CoAl . With increasing the Mn(A or B site) \leftrightarrow Co(C site) disorder in XA -type Mn_2CoAl , the value of I_{002}/I_{004} near the Mn K absorption edge gradually decreases, leading to the disappearance of a peak [Fig. 5(a)]. In addition, the shape of a peak for I_{111}/I_{004} near the Mn K absorption edge changes from convex upward to downward [Fig. 5(b)]. Considering these features, one can discuss the exact atomic-level ordered structure of the experimentally obtained Mn_2CoAl [35,58].

Also in Figs. 5(a) and 5(b), we plot the experimentally obtained AXRD data for I_{002}/I_{004} and I_{111}/I_{004} near the Mn K absorption edge of the 100 °C-grown Mn_2CoAl film with a thickness of 15 nm as red circles. By a comparison of I_{002}/I_{004} between the calculation and the experiment, we can recognize the absence of the Mn(B site) \leftrightarrow Co(C site) disorder, tentatively indicating the presence of the XA -type structure in the 100 °C-grown Mn_2CoAl film. In Fig. 5(b) the detailed comparisons of I_{111}/I_{004} between the calculation and the

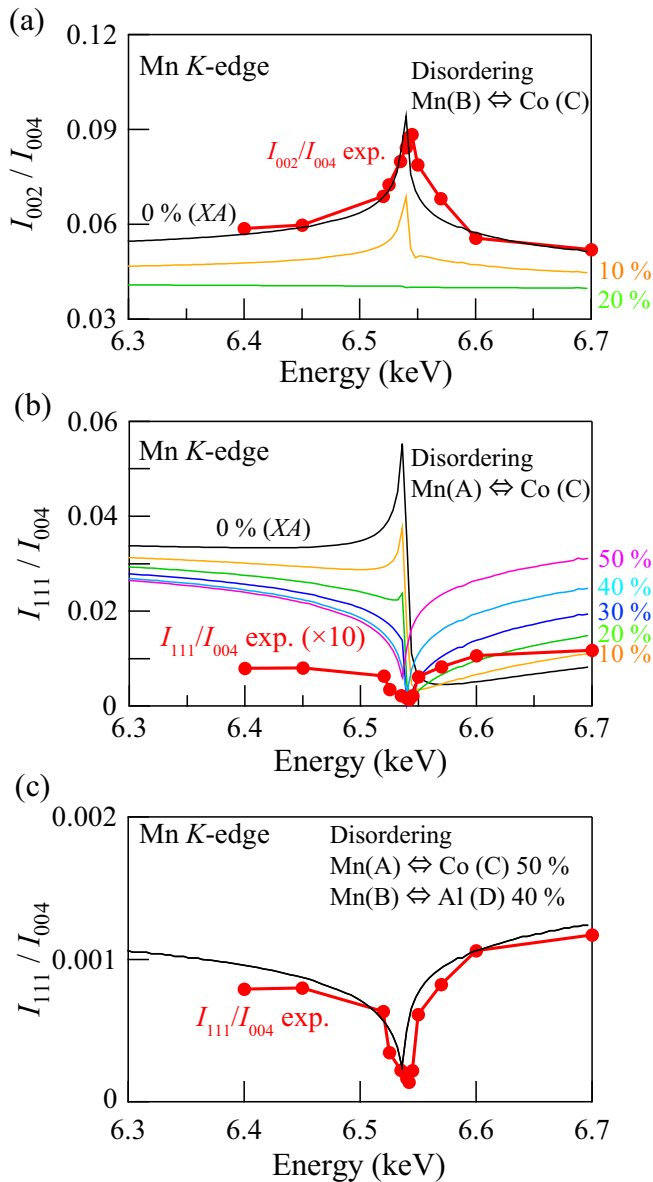


FIG. 5. X-ray energy dependence of the calculated and experimental (a) I_{002}/I_{004} with the Mn(B site) \leftrightarrow Co(C site) disorder and (b) I_{111}/I_{004} with the Mn(A site) \leftrightarrow Co(C site) disorder near the Mn K absorption edge. (c) Comparison of I_{111}/I_{004} between the experiment and the calculation with the presence of the 40% Mn(B site) \leftrightarrow Al(D site) swapping, together with the 50% Mn(A site) \leftrightarrow Co(C site) swapping.

experiment can verify the presence of the Mn(A site) \leftrightarrow Co(C site) disorder. Although the shape of the experimental data for I_{111}/I_{004} is similar to the calculation with the presence of the 50% Mn(A site) \leftrightarrow Co(C site) disorder ($L2_1B$ -type structure [36,37]) in XA-type Mn_2CoAl , its intensity cannot be reproduced precisely. Here we recall the degrees of $B2$ and $L2_1$ ordering, $S_{B2} \sim 1$ and $S_{L2_1} \sim 0.4$, respectively, in Fig. 1. Because the value of S_{L2_1} is relatively low, we should also take into account the presence of the Mn(B site) \leftrightarrow Al(D site) disorder. Considering this fact, we show the calculated intensity of I_{111}/I_{004} with the presence of both the 50% Mn(A site) \leftrightarrow Co(C site) disorder and the 40% Mn(B site) \leftrightarrow Al(D

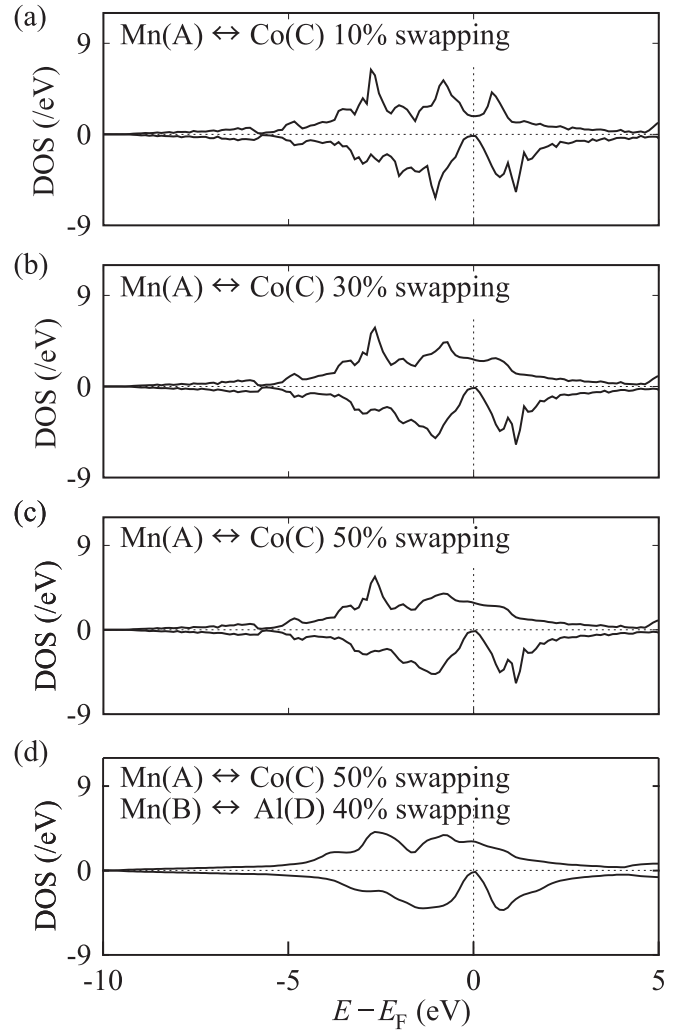


FIG. 6. Spin-resolved total density of states (DOS) of $L2_1B$ -type Mn_2CoAl in the presence of (a) 10%, (b) 30%, and (c) 50% Mn(A site) \leftrightarrow Co(C site) swapping. (d) Spin-resolved total DOS of disordered $L2_1B$ -type Mn_2CoAl in the presence of both the 50% Mn(A site) \leftrightarrow Co(C site) swapping and the 40% Mn(B site) \leftrightarrow Al(D site) swapping.

site) disorder in Fig. 5(c). As a result, the shape and intensity of the experimental data for I_{111}/I_{004} are well reproduced. Given the structural characterizations in Figs. 1 and 5, we can determine the crystal structure of the 100 °C-grown Mn_2CoAl films to be a disordered $L2_1B$ -type structure including the 50% Mn(A site) \leftrightarrow Co(C site) swapping and the 40% Mn(B site) \leftrightarrow Al(D site) swapping.

E. Electronic band structures

To discuss the electronic band structure in the disordered $L2_1B$ -type Mn_2CoAl in detail, we use the Akai-KKR program package [59], in which the Korringa-Kohn-Rostoker (KKR) Green's function method is implemented within density functional theory. The spin polarization with the semirelativistic calculations is considered. A total of 195 independent k points is sampled in the first Brillouin zone. The Moruzzi-Janak-Williams potential is used for the exchange-correlation calculations [60]. The disordered structures are treated in

TABLE I. Comparison of structural characterization, electric, and magnetic properties of bulk and thin-film Mn₂CoAl.

Sample	Method	Structure	Magnetic moment (μ_B /f.u.)	Temperature dependence of ρ	n or p (cm ⁻³)	σ_{AHC} (S/cm)	MR sign
Bulk [10]	Arc melting (Unknown)	Unknown	2.0 (<5 K)	Negative	1.7×10^{20} (2 K) n -type [62]	22 (2 K)	Positive (≤ 100 K)
Bulk [35]	Arc melting (1100 °C)	Multiphase with disordered XA	2.6 (5 K)	Negative	$\sim 2.9 \times 10^{22}$ (10 K) p -type	25 (10 K)	—
[001]-oriented film [29]	Sputtering (400 °C)	$B2$	~ 1.9 (5 K)	Negative	1.6×10^{20} (5 K) p -type	~ 5.0 (5 K)	Negative
Epitaxial film [30]	Sputtering (500 °C)	$B2$	1.0 (Room temperature)	Negative	2.0×10^{21} p -type	78 (5 K)	Negative
Epitaxial film [31]	Sputtering (400 °C)	$B2$	~ 1.8 (Room temperature)	Negative	6.0×10^{20} (4 K) p -type	~ 25 (4 K)	Negative
Epitaxial film [34]	Sputtering (550 °C)	$B2$	~ 1.0 (10 K)	Negative	2.0×10^{22} p -type	—	Negative
Epitaxial film [28]	MBE (325 °C)	Disordered $L2_1$ ($S_{B2} \sim 0.43$)	1.0 (10 K)	Positive (≤ 200 K) Negative (> 200 K)	4.0×10^{22} (Room temperature) n -type	12 (Room temperature)	Negative
Epitaxial film [32]	MBE (300 °C)	Disordered $L2_1$ [58]	~ 1.9 (10 K)	Negative	$\sim 1.2 \times 10^{22}$ (10 K) p -type	~ 8.9 (10 K)	Negative
Epitaxial film [33]	MBE (150 °C)	$B2$ ($S_{B2} \sim 0.89$)	—	Negative	—	—	Negative
Epitaxial film (this study)	MBE (100 °C)	Single-phase disordered $L2_1B$	~ 2.0 (10 K)	Negative	$\sim 2.0 \times 10^{22}$ (10 K) p -type	~ 16 (10 K)	Positive (10 K)

accordance with the coherent potential approximation (CPA) [61], in which the supercell method is not necessary because the multipole scattering effect is replaced by an effective-medium potential. Prior to the calculation for the disordered $L2_1B$ -type Mn₂CoAl having some amount of Mn(A site) \Leftrightarrow Co(C site) swapping and Mn(B site) \Leftrightarrow Al(D site) swapping, we first confirmed the spin-resolved total density of states (DOS) for an XA -type structure, where the concentration of Co atoms at the A site was assumed to be 0%. As a result, although a small number of states were spilled into the gap due to CPA, the calculated total DOS reproduced an SGS-like electronic band structure (not shown here) like that found in previous works [10,27,36].

Using this reliable method, we next calculate the DOSs for various concentrations of the swapping between Mn(A site) and Co(C site) to consider the experimental results in Fig. 5. Figures 6(a), 6(b) and 6(c) display the total DOS for $L2_1B$ -type Mn₂CoAl with 10%, 30%, and 50% Mn(A site) \Leftrightarrow Co(C site) swapping, respectively. In these cases, the calculated magnetic moments are estimated to be $2.01 \mu_B$ /f.u. for Fig. 6(a), $2.01 \mu_B$ /f.u. for Fig. 6(b), and $2.02 \mu_B$ /f.u. for Fig. 6(c), respectively. These results are consistent with our experimental results shown in the inset in Fig. 3(a). In addition, the results for 50% Mn(A site) \Leftrightarrow Co(C site) swapping agree well with a previous work by Xin *et al.* [36], although the calculation methods in this work are different from those in Ref. [36]. Notably, although the gapless-like DOS structure of the majority spins gradually disappears with increasing the amount of Mn(A site) \Leftrightarrow Co(C site) swapping and becomes toward the metallic-like structure, that of the minority spins remains even in the presence of the 50% Mn(A site) \Leftrightarrow Co(C site) swapping. Namely, the Mn(A site) \Leftrightarrow Co(C site)

swapping in $L2_1B$ -type Mn₂CoAl influences the electronic band structure only for the majority spins. Last, the influence of the Mn(B site) \Leftrightarrow Al(D site) swapping on the electronic structure is considered in Fig. 6(d). As a result, the gapless-like DOS structure of the minority spins still remains even for the disordered $L2_1B$ -type structure including the 40% Mn(B site) \Leftrightarrow Al(D site) swapping in addition to the 50% Mn(A site) \Leftrightarrow Co(C site) swapping. Even in this case, the magnetic moment is theoretically calculated to be $2.01 \mu_B$ /f.u. From these theoretical calculations, it is found that spin-gapless half-metals such as Fe₂CoSi [50] are realized for the 100 °C-grown Mn₂CoAl films in this study.

IV. DISCUSSION

To compare recent results for Mn₂CoAl, we summarize the reported structural, electrical, and magnetic properties for bulk [10,35] and thin-film [28–34] Mn₂CoAl in Table I. From these comparisons, although all of the reports have so far shown a reasonable magnetic moment, weak negative temperature-dependent ρ , and low σ_{AHC} , there has been almost no correlation between them and the formation of the XA -type structure. In addition to the above situation, only two studies, including this work, have shown the PLMR effect, which may be due to the quantum linear MR effect related to the gapless-like special electronic structure near the Fermi level [18,48].

Since homogeneous and single-phase Mn₂CoAl epitaxial films have been demonstrated in this study, the correlation between the presence of the PLMR effect and the atomic-level ordered structure can be considered. Taking into account the previous works [10,50] and the results in Fig. 6, we can first

discuss that the PLMR effect observed in the disordered $L2_1B$ -type Mn_2CoAl epitaxial films originates from the quantum linear MR effect due to the gapless electronic band structure related to the minority states near the Fermi level. Recently, although the PLMR effect due to the quantum linear MR effect was also observed for the partially disordered $CoFeVSi$ Heusler alloy [23,25], the magnitude of the PLMR was quite small because of the presence of large carrier concentrations due to the $Co \leftrightarrow Fe$ disorder. For the disordered $L2_1B$ -type Mn_2CoAl epitaxial films, the magnitude of the PLMR in Fig. 4 is also small compared to that for the bulk Mn_2CoAl [10]. We infer that the small PLMR effect is affected by the presence of the low carrier mobility ($\sim 0.6 \text{ cm}^2/\text{Vs}$) arising from impurity and/or spin-dependent scattering in the large DOS of the majority spins. Next, we can consider the realization of a conventional half-metallic property with a very small energy gap [63]. If a half-metallic electronic band structure with a small energy gap less than several meV was realized in disordered $L2_1B$ -type Mn_2CoAl epitaxial films, the spin-magnon scattering could be expected to freeze out only at low temperatures less than 10 K. Similar features have already been observed in a famous half-metal, $L2_1$ -type Co_2FeSi , with a small energy gap [63]. Thus, there are several possibilities of the mechanism of the manifestation for the PLMR effect even in disordered $L2_1B$ -type Mn_2CoAl epitaxial films.

On the basis of these considerations, we conclude that the observation of the PLMR effect is not evidence of the formation of XA -type Mn_2CoAl . We suggest that it is effective to perform disorder-sensitive structural analyses such as AXRD [35,53–55,58] and extended x-ray absorption fine structure (EXAFS) [64–67] to obtain evidence of the formation of the XA -type structure. Furthermore, the values of the carrier concentration shown in Table I are largely scattered from sample to sample, which are not consistent with the quality of Mn_2CoAl samples. The carrier concentration for all the samples should be estimated accurately from Hall-effect measurements of fabricated Hall-bar devices.

V. CONCLUSION

The belief has been that the PLMR effect at low temperatures in Mn_2CoAl originates from the quantum linear MR effect in the gapless electronic band structures near the Fermi level, which is likely to be evidence of the realization

of the XA -type structure [10]. Although lots of Mn_2CoAl films have been reported, a detailed discussion of the correlation between the PLMR effect and the presence of the XA -type structure has not been shown yet. In this paper, we observed the PLMR effect at 10 K in homogeneous and single-phase Mn_2CoAl epitaxial films grown by MBE at 100°C in addition to a reasonable magnetic moment, weak negative temperature-dependent ρ , and low σ_{AHC} . However, from AXRD measurements and their analyses, we found that the 100°C -grown Mn_2CoAl epitaxial film is not an XA -type structure but is a disordered $L2_1B$ -type structure having some amount of $Mn(\text{A site}) \leftrightarrow Co(\text{C site})$ swapping and $Mn(\text{B site}) \leftrightarrow Al(\text{D site})$ swapping. On the basis of first-principles density-functional theory calculations, we conclude that the PLMR effect observed in the disordered $L2_1B$ -type Mn_2CoAl epitaxial films originates from the quantum linear MR effect due to the gapless electronic band structure related to the minority states near the Fermi level or from the freeze-out of the spin-magnon scattering due to the half-metallic electronic band structure with a small energy gap less than several meV. Namely, there is still no direct evidence of the SGS-like band structure related to the PLMR effect at low temperatures because the PLMR effect can also occur from spin-gapless half-metals such as Fe_2CoSi [50] and $CoFeVSi$ [23,25] or conventional half-metals with a small energy gap such as Co_2FeSi [63]. To obtain definite evidence of the formation of the XA -type structure, element-specific and disorder-sensitive structural analyses such as AXRD and EXAFS, even for bulk Mn_2CoAl , are effective.

ACKNOWLEDGMENTS

This work was partly supported by JSPS KAKENHI (Grants No. 17H06152, No. 18KK0111, and No. 19H05616), JST-CREST (Grant No. JPMJCR18J1), the Nippon Sheet Glass Foundation for Materials Science and Engineering, and the Spintronics Research Network of Japan (Spin-RNJ). K.K. acknowledges JSPS Research Fellowships for Young Scientists (Grant No. 20J10124). The computation was performed at the Supercomputer Center, Institute for Solid State Physics, The University of Tokyo. The synchrotron radiation experiments were performed on beamline BL13XU at SPring-8 with the approval of the JASRI (Proposals No. 2019B2080, No. 2019A0927, and No. 2019B1657).

-
- [1] X. L. Wang, *Phys. Rev. Lett.* **100**, 156404 (2008).
 - [2] X. L. Wang, S. X. Dou, and C. Zhang, *NPG Asia Mater.* **2**, 31 (2010).
 - [3] I. Žutić, J. Fabian, and S. D. Sarma, *Rev. Mod. Phys.* **76**, 323 (2004).
 - [4] E. Şaşıoğlu, T. Aull, D. Kutschabsky, S. Blügel, and I. Mertig, *Phys. Rev. Appl.* **14**, 014082 (2020).
 - [5] E. Şaşıoğlu, S. Blügel, and I. Mertig, *ACS Appl. Electron. Mater.* **1**, 1552 (2019).
 - [6] D. H. Kim, J. Hwang, E. Lee, K. J. Lee, S. M. Choo, M. H. Jung, J. Baik, H. J. Shin, B. Kim, K. Kim, B. I. Min, and J.-S. Kang, *Appl. Phys. Lett.* **104**, 022411 (2014).
 - [7] Y. Li, Z. Zhou, P. Shen, and Z. Chen, *ACS Nano* **3**, 1952 (2009).
 - [8] F.-B. Zheng, C.-W. Zhang, P.-J. Wang, and S.-S. Li, *J. Appl. Phys.* **113**, 154302 (2013).
 - [9] Y. Liu, S. K. Bose, and J. Kudrnovský, *J. Magn. Magn. Mater.* **423**, 12 (2017).
 - [10] S. Ouardi, G. H. Fecher, C. Felser, and J. Kübler, *Phys. Rev. Lett.* **110**, 100401 (2013).
 - [11] S. Skaftouros, K. Özdoğan, E. Şaşıoğlu, and I. Galanakis, *Appl. Phys. Lett.* **102**, 022402 (2013).
 - [12] G. Y. Gao and K.-L. Yao, *Appl. Phys. Lett.* **103**, 232409 (2013).
 - [13] G. Z. Xu, E. K. Liu, Y. Du, G. J. Li, G. D. Liu, W. H. Wang, and G. H. Wu, *Europhys. Lett.* **102**, 17007 (2013).

- [14] H. Y. Jia, X. F. Dai, L. Y. Wang, R. Liu, X. T. Wang, P. P. Li, Y. T. Cui, and G. D. Liu, *AIP Adv.* **4**, 047113 (2014).
- [15] L. Bainsla and K. G. Suresh, *Appl. Phys. Rev.* **3**, 031101 (2016).
- [16] X. Wang, Z. Cheng, J. Wang, X.-L. Wang, and G. Liu, *J. Mater. Chem. C* **4**, 7176 (2016).
- [17] Q. Gao, I. Opahle, and H. Zhang, *Phys. Rev. Mater.* **3**, 024410 (2019).
- [18] A. A. Abrikosov, *Phys. Rev. B* **58**, 2788 (1998); *Europhys. Lett.* **49**, 789 (2000).
- [19] X. L. Wang, G. Peleckis, C. Zhang, H. Kimura, and S. Dou, *Adv. Mater.* **21**, 2196 (2009).
- [20] L. Bainsla, K. G. Suresh, A. K. Nigam, M. M. Raja, B. S. D. Ch. S. Varaprasad, Y. K. Takahashi, and K. Hono, *J. Appl. Phys.* **116**, 203902 (2014).
- [21] L. Bainsla, A. I. Mallick, M. M. Raja, A. K. Nigam, B. S. D. Ch. S. Varaprasad, Y. K. Takahashi, A. Alam, K. G. Suresh, and K. Hono, *Phys. Rev. B* **91**, 104408 (2015).
- [22] L. Bainsla, A. I. Mallick, M. M. Raja, A. A. Coelho, A. K. Nigam, D. D. Johnson, A. Alam, and K. G. Suresh, *Phys. Rev. B* **92**, 045201 (2015).
- [23] S. Yamada, S. Kobayashi, F. Kuroda, K. Kudo, S. Abo, T. Fukushima, T. Oguchi, and K. Hamaya, *Phys. Rev. Materials* **2**, 124403 (2018).
- [24] Y. Venkateswara, S. Gupta, S. S. Samatham, M. R. Varma Enamullah, K. G. Suresh, and A. Alam, *Phys. Rev. B* **97**, 054407 (2018).
- [25] S. Yamada, S. Kobayashi, A. Masago, L. S. R. Kumara, H. Tajiri, T. Fukushima, S. Abo, Y. Sakuraba, K. Hono, T. Oguchi, and K. Hamaya, *Phys. Rev. B* **100**, 195137 (2019).
- [26] D. Rani Enamullah, L. Bainsla, K. G. Suresh, and A. Alam, *Phys. Rev. B* **99**, 104429 (2019).
- [27] I. Galanakis, K. Özdoğan, E. Şaşıoğlu, and S. Blügel, *J. Appl. Phys.* **115**, 093908 (2014).
- [28] M. E. Jamer, B. A. Assaf, T. Devakul, and D. Heiman, *Appl. Phys. Lett.* **103**, 142403 (2013).
- [29] G. Z. Xu, Y. Du, X. M. Zhang, H. G. Zhang, E. K. Liu, W. H. Wang, and G. H. Wu, *Appl. Phys. Lett.* **104**, 242408 (2014).
- [30] N. Y. Sun, Y. Q. Zhang, H. R. Fu, W. R. Che, C. Y. You, and R. Shan, *AIP Adv.* **6**, 015006 (2016).
- [31] K. Ueda, S. Hirose, and H. Asano, *Appl. Phys. Lett.* **110**, 202405 (2017).
- [32] K. Arima, F. Kuroda, S. Yamada, T. Fukushima, T. Oguchi, and K. Hamaya, *Phys. Rev. B* **97**, 054427 (2018).
- [33] P. Chen, C. Gao, G. Chen, K. Mi, M. Liu, P. Zhang, and D. Xue, *Appl. Phys. Lett.* **113**, 122402 (2018).
- [34] R. G. Buckley, T. Butler, C. Pot, N. M. Strickland, and S. Granville, *Mater. Res. Express* **6**, 106113 (2019).
- [35] X. D. Xu, Z. X. Chen, Y. Sakuraba, A. Perumal, K. Masuda, L. S. R. Kumara, H. Tajiri, T. Nakatani, J. Wang, W. Zhou, Y. Miura, T. Ohkubo, and K. Hono, *Acta Mater.* **176**, 33 (2019).
- [36] Y. Xin, H. Hao, Y. Ma, H. Luo, F. Meng, H. Liu, E. Liu, and G. Wu, *Intermetallics* **80**, 10 (2017).
- [37] R. Y. Umetsu, M. Tsujikawa, K. Saito, K. Ono, T. Ishigaki, R. Kainuma, and M. Shirai, *J. Phys.: Condens. Matter* **31**, 065801 (2019).
- [38] K. Hamaya, H. Itoh, O. Nakatsuka, K. Ueda, K. Yamamoto, M. Itakura, T. Taniyama, T. Ono, and M. Miyao, *Phys. Rev. Lett.* **102**, 137204 (2009).
- [39] K. Tanikawa, S. Oki, S. Yamada, M. Kawano, M. Miyao, and K. Hamaya, *Thin Solid Films* **557**, 390 (2014).
- [40] S. Yamada, K. Tanikawa, S. Oki, M. Kawano, M. Miyao, and K. Hamaya, *Appl. Phys. Lett.* **105**, 071601 (2014).
- [41] Y. Fujita, M. Yamada, M. Tsukahara, T. Oka, S. Yamada, T. Kanashima, K. Sawano, and K. Hamaya, *Phys. Rev. Appl.* **8**, 014007 (2017).
- [42] K. Kudo, S. Yamada, J. Chikada, Y. Shimanuki, T. Ishibe, S. Abo, H. Miyazaki, Y. Nishino, Y. Nakamura, and K. Hamaya, *Phys. Rev. B* **99**, 054201 (2019).
- [43] Y. Takamura, R. Nakane, and S. Sugahara, *J. Appl. Phys.* **105**, 07B109 (2009).
- [44] Y. Takamura, T. Suzuki, Y. Fujino, and S. Nakagawa, *J. Appl. Phys.* **115**, 17C732 (2014).
- [45] T. Block, C. Felser, G. Jakob, J. Enslin, B. Mühlning, P. Gütllich, and R. J. Cava, *J. Solid State Chem.* **176**, 646 (2003).
- [46] S. Majumdar, M. K. Chattopadhyay, V. K. Sharma, K. J. S. Sokhey, S. B. Roy, and P. Chaddah, *Phys. Rev. B* **72**, 012417 (2005).
- [47] J.-P. Jan, *Solid State Phys.* **5**, 1 (1957).
- [48] R. Xu, A. Husmann, T. F. Rosenbaum, M.-L. Saboungi, J. E. Enderby, and P. B. Littlewood, *Nature (London)* **390**, 57 (1997).
- [49] M. Lee, T. F. Rosenbaum, M.-L. Saboungi, and H. S. Schnyders, *Phys. Rev. Lett.* **88**, 066602 (2002).
- [50] Y. Du, G. Z. Xu, X. M. Zhang, Z. Y. Liu, S. Y. Yu, E. K. Liu, W. H. Wang, and G. H. Wu, *Europhys. Lett.* **103**, 37011 (2013).
- [51] T. Liang, Q. Gibson, M. N. Ali, M. Liu, R. J. Cava, and N. P. Ong, *Nat. Mater.* **14**, 280 (2015).
- [52] A. L. Friedman, J. L. Tedesco, P. M. Campbell, J. C. Culbertson, E. Aifer, F. K. Perkins, R. L. Myers-Ward, J. K. Hite, C. R. Eddy, Jr., G. G. Jernigan, and D. K. Gaskill, *Nano Lett.* **10**, 3962 (2010).
- [53] B. Ravel, J. O. Cross, M. P. Raphael, V. G. Harris, R. Ramesh, and V. Saraf, *Appl. Phys. Lett.* **81**, 2812 (2002).
- [54] S. Li, Y. K. Takahashi, Y. Sakuraba, N. Tsuji, H. Tajiri, Y. Miura, J. Chen, T. Furubayashi, and K. Hono, *Appl. Phys. Lett.* **108**, 122404 (2016).
- [55] S. Li, T. Nakatani, K. Masuda, Y. Sakuraba, X. D. Xu, T. T. Sasaki, H. Tajiri, Y. Miura, T. Furubayashi, and K. Hono, *Acta Mater.* **142**, 49 (2018).
- [56] O. Sakata, Y. Furukawa, S. Goto, T. Mochizuki, T. Uruga, K. Takeshita, H. Ohashi, T. Ohata, T. Matsushita, S. Takahashi, H. Tajiri, T. Ishikawa, M. Nakamura, M. Ito, K. Sumitani, T. Takahashi, T. Shimura, A. Saito, and M. Takahashi, *Surf. Rev. Lett.* **10**, 543 (2003).
- [57] H. Tajiri, H. Yamazaki, H. Ohashi, S. Goto, O. Sakata, and T. Ishikawa, *J. Synchrotron Radiat.* **26**, 750 (2019).
- [58] H. Tajiri, L. S. R. Kumara, Y. Sakuraba, Z. Chen, J. Wang, W. Zhou, K. Varun, S. Yamada, K. Ueda, K. Hamaya, and K. Hono, *arXiv:2012.12282*.
- [59] H. Akai, *J. Phys. Soc. Jpn.* **51**, 468 (1982).
- [60] V. L. Moruzzi, J. F. Janak, and A. R. Williams, *Calculated Electronic Properties of Metals* (Pergamon, Oxford, 1978).
- [61] G. M. Stocks, W. M. Temmerman, and B. L. Gyorffy, *Phys. Rev. Lett.* **41**, 339 (1978).
- [62] S. Ouardi, G. H. Fecher, C. Felser, and J. Kübler, *Phys. Rev. Lett.* **122**, 059901(E) (2019).
- [63] D. Bombor, C. G. F. Blum, O. Volkonskiy, S. Rodan, S. Wurmehl, C. Hess, and B. Büchner, *Phys. Rev. Lett.* **110**, 066601 (2013).
- [64] B. Ravel, M. P. Raphael, V. G. Harris, and Q. Huang, *Phys. Rev. B* **65**, 184431 (2002).

- [65] S. Wurmehl, G. H. Fecher, H. C. Kandpal, V. Ksenofontov, C. Felser, H.-J. Lin, and J. Morais, [Phys. Rev. B **72**, 184434 \(2005\)](#).
- [66] S. Ouardi, G. H. Fecher, B. Balke, A. Beleanu, X. Kozina, G. Stryganyuk, C. Felser, W. Klöß, H. Schrader, F. Bernardi, J. Morais, E. Ikenaga, Y. Yamashita, S. Ueda, and K. Kobayashi, [Phys. Rev. B **84**, 155122 \(2011\)](#).
- [67] D. Rani, J. Kangsabanik, K. G. Suresh, N. Patra, D. Bhattacharyya, S. N. Jha, and A. Alam, [Phys. Rev. Appl. **10**, 054022 \(2018\)](#).